PHYSICAL REVIEW E **82**, 021507 (2010)

Binary fluid with attractions near a planar wall

Venkat Padmanabhan,[1] Amalie L. Frischknecht,[2] and Michael E. Mackay[1]
[1]*Department of Materials Science and Engineering, University of Delaware, Newark, Delaware 19716, USA*
[2]*Center for Integrated Nanotechnologies, Sandia National Laboratories, Albuquerque, New Mexico 87185, USA*

(Received 11 November 2009; revised manuscript received 10 May 2010; published 12 August 2010)

It is well known that a mixture of big and small hard spheres next to a planar wall will exhibit segregation based on their size difference. The larger spheres will tend to locate next to the substrate because the overall system entropy loss per unit area is less. In the present study we determine the role of attraction between the small particles and the wall to displace the larger particles. Both fluids density-functional theory and discontinuous molecular dynamics simulations demonstrate that at a certain attractive potential, which is on the order of the thermal energy, the large particles can indeed be dislodged from the surface layer so the small particles are now the major surface component. Exploration of a range of parameters, including relative sphere size and concentration, as well as attractions between the small spheres in the bulk, shows that the phenomenon is quite robust.

DOI: 10.1103/PhysRevE.82.021507 PACS number(s): 64.75.Gh, 64.75.Yz

I. INTRODUCTION

In a fluid mixture of colloidal particles, the distribution of the particles near a substrate is determined by the complex interplay among the steric effects and the particular particle-wall and particle-particle interactions [1]. Understanding the various contributions to the surface free energy is both a fundamental issue in colloid science, and necessary for controlling particle distributions in a variety of self-assembled fluid systems. If all the fundamental forces acting on a collection of particles at any given surface were known, it would be possible to design systems so that particles assembled in desired locations. An example of a step in this direction is self-assembly of a polymer-nano-particle system [2], in which the nanoparticles segregated to the solid substrate when the entropic forces were dominant or to the air interface if the dielectric properties were properly tuned.

The simplest example of fluid particle mixtures is a binary mixture of hard spheres, in which the particle distribution near a hard substrate is determined only by entropic contributions to the surface free energy. Binary hard sphere mixtures have been extensively studied in the literature, both experimentally [3] and theoretically [4–9]. It has been shown that when there is a size anisotropy, there is an effective "depletion" attraction between the large spheres caused by the presence of the small spheres [10,11]. As shown in Fig. 1, the centers of the small spheres are excluded from being closer than half their diameter from the surface of the large spheres, so that there is no overlap. When two large spheres are close enough for their depletion layers to overlap, the effective volume accessible to the small spheres increases. This increase in volume, due to such overlapping depletion zones, leads to an increase in the small spheres' translational entropy, which induces a depletion attraction between the big spheres. For sufficiently large size ratios $\xi=\sigma_b/\sigma_s=5$ (where σ_b and σ_s are the diameters of the big and small spheres, respectively), it has been observed that a metastable fluid-fluid phase separation exists within a stable solid-fluid coexistence boundary by virtue of this depletion attraction [12,13].

In the presence of a hard substrate (wall), the depletion zone also exists along the surface of the wall. This results in a similar depletion attraction between the wall and the big spheres, leading to an enhancement of the big particle density close to the wall [14,15]. This leads to a fundamental question: what is required to overcome the entropic depletion interaction pushing the large particles to the wall? In this paper, we show that adding an attractive interaction between the small spheres and the wall is sufficient to displace the large particles from the wall. We also show that the wall-small sphere attraction remains sufficient to displace the large particles when we also add a fluid-fluid attractive interaction between the small spheres.

To do so, we use classical density-functional theory (DFT). DFT has been shown to very accurately describe the statistical mechanics of hard spheres [16] and hard sphere mixtures near surfaces [17]. In particular, Roth and Dietrich [10] calculated the structural and thermodynamic properties of binary hard-sphere mixtures near a hard wall with two different size ratios using DFT, and showed excellent agreement with simulation. The DFT accurately captured the depletion effect for these mixtures, for three different versions of the Rosenfeld density functional.

In this paper, we use the "White-Bear" functional [18] that provides slightly more accurate density profiles, especially near contact, of hard sphere mixtures near a planar hard wall. It has been shown by comparison with simulation

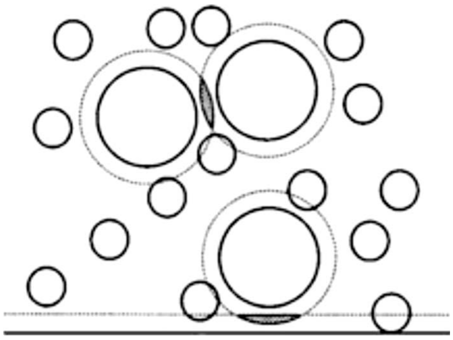

FIG. 1. The depletion effect. Continuous lines represent the large and small hard spheres and a hard wall. Dotted lines delineate the depletion zones inside of which the center of a small sphere is excluded. Hatched areas represent overlapping depletion zones.

that DFT also usually works well for hard-sphere or repulsive fluids near an attractive wall [19–21]. We verify the accuracy of the DFT for our binary mixtures with small particle-wall attractions by also performing discontinuous molecular dynamics (DMD) simulations on the same systems. An additional goal of performing DMD simulations is to add to the available simulation data, which is still somewhat scarce in the literature for binary mixtures. We study the effects of attractions between the small particles by combining the hard-sphere White-Bear functional with a mean-field description of the attractions. It is well-known that the mean-field form of the attractions is problematic in DFT, and is particularly inaccurate for fluids near critical points [22] and for attractive fluids near neutral or repulsive walls [22–24]. Here, we show that the DFT is in good agreement with DMD simulations for systems which are far from any binodals, and which have a particle-wall attraction as well as the fluid-fluid attraction for the small particles.

We investigate binary mixtures at several compositions, at finite volume fractions of both spheres. There has been some work in the literature that also looked at the effects of attractions in binary sphere mixtures, but those studies that focused on the depletion potential were all done in the dilute limit, with 1 or 2 large spheres in a sea of small spheres [25]. Most of the other work in this area used the Asakura-Oosawa (AO) approximation, used to model mixtures of colloids and nonadsorbing polymers. In the AO approximation, the polymers are treated as hard spheres in their interactions with the colloids, but the polymer-polymer interactions are those of an ideal gas [26–28]. In this work, we do not make such assumptions, but rather consider small particles with excluded volume. We show that as we increase the strength of attraction (ε_{wf}) between the small spheres and the wall, the small sphere density near the wall increases by pushing the big spheres away. There is a transitional value, ε_{wf}^{*}, beyond which the concentration of the small spheres at the wall is higher than that of the big spheres.

The content of the paper is organized as follows. In Sec. II we first introduce the model in Sec. II A and then briefly describe the details of the DMD simulations and the DFT in Secs. II B and II C, respectively. We present our results in Sec. III, starting with the effects of a small sphere-wall attraction in Sec. III A and continuing with the effects of adding fluid-fluid attractions between the small spheres in Sec. III B. We summarize our findings in Sec. IV.

II. MODEL AND METHODS

A. Model

We study a mixture of hard spheres with diameters σ_s and σ_b. In all of our calculations the fluid-fluid interaction for the big spheres and between big and small spheres is hard-core, with $\sigma_{\mathrm{bs}}=(\sigma_{\mathrm{b}}+\sigma_{\mathrm{s}})/2$. Additionally, the big spheres have purely hard interactions with the wall. We model the attractive interactions between the small spheres and the wall by a square well potential. The wall-fluid potential for the small spheres is thus given by

$$V(x)=\begin{cases}\infty; & x<\dfrac{\sigma_s}{2}\\[2ex] -\varepsilon_{wf}; & \dfrac{\sigma_s}{2}\le x\le\lambda\\[2ex] 0; & x>\lambda,\end{cases}\tag{1}$$

where x is the perpendicular distance of the small sphere from the wall. The walls are smooth and extend infinitely in the y and z directions. ε_{wf} is the well depth and λ is the potential range. In the calculations presented here, $\lambda=1.5\sigma_s$ unless otherwise specified. The wall-fluid attraction strength was varied from $\varepsilon_{wf}=0.2$ to 2.0 kT.

We also investigate the effect of adding small sphere-small sphere attractions. The fluid-fluid potential for the small spheres is also a square-well potential given by

$$u(r)=\begin{cases}\infty; & r<\sigma_s\\ -\varepsilon_{ff}; & \sigma_s\le r\le\lambda\\ 0; & r>\lambda,\end{cases}\tag{2}$$

where r is the distance between any two attractive particles. ε_{ff} is the fluid-fluid attraction strength and $\lambda=1.5\sigma_s$ is the potential range. Fluid-fluid attractions were investigated by increasing ε_{ff} from 0.0 to 0.4 kT for every value of ε_{wf}.

We consider systems with size ratios $\xi=2$, 3, and 4. These size ratios are less than the size asymmetry required to induce phase separation, so our mixtures are miscible in the bulk. The total packing fraction, $\eta=\pi/6(\rho_b\sigma_b^3+\rho_s\sigma_s^3)$, was kept at solutionlike densities. Here, $\rho_{\mathrm{s/b}}$ are the small and big number densities, and we define $\eta_i=\pi\rho_i\sigma_i^3/6$ for i=s,b as the individual small and big particle packing fractions. We focus on systems with a volume fraction of small particles of $\Phi_s\approx0.22$, which corresponds to a larger number density of small particles than large particles due to the size asymmetries. For the $\xi=2$ case, we consider two additional compositions with volume fractions of the small particles $\Phi_s\approx0.14$ and $\Phi_s\approx0.66$. We present additional DFT results for all three size ratios at $\Phi_s=0.128$. Since the DMD simulations necessarily involved finite numbers of particles, an unknown number of which were adsorbed near the wall, the packing fractions in the bulk region far from the wall differed somewhat for different values of ε_{wf}. The total packing fraction and the individual species packing fractions for all the cases studied are given in Table I.

B. Discontinuous molecular dynamics

We simulate the binary fluid mixture by using the DMD method [29–31]. Traditional molecular dynamics employs a particle-particle interaction potential that is a continuous function of particle separation (for example, the Lennard-Jones potential), and which incorporates short-range repulsions as well as long-range attractions. The trajectories of a system of particles are repeatedly advanced at a small increment in time, after which the forces between all pairs of particles are reevaluated. DMD, on the other hand, replaces the continuous potential function with a discontinuous function, such as a hard-sphere repulsion or square-well attraction.

TABLE I. Total (η) and individual packing fractions for small (η_s) and big (η_b) particles for different size ratios ξ and small particle volume fractions Φ_s. For $\xi=2$ and each individual value of ε_{wf}, the first row is for $\Phi_s \approx 0.22$, the second row for $\Phi_s \approx 0.66$, and the third row for $\Phi_s \approx 0.14$.

ξ	η	Φ_s	η_s	η_b	ε_{wf}	ε_{ff}
2	0.387	0.222	0.086	0.301	0.0	0.0
	0.363	0.656	0.238	0.125		
	0.350	0.143	0.050	0.300		
	0.388	0.216	0.084	0.304	0.2	
	0.337	0.658	0.222	0.115		
	0.358	0.139	0.050	0.308		
	0.387	0.219	0.085	0.302	0.34	
	0.358	0.672	0.238	0.120		
	0.359	0.134	0.048	0.311		
	0.388	0.214	0.083	0.305	0.5	
	0.344	0.663	0.228	0.116		
	0.374	0.131	0.049	0.325		
	0.393	0.196	0.077	0.316	0.67	
	0.348	0.681	0.237	0.111		
	0.367	0.136	0.050	0.317		
	0.393	0.193	0.076	0.317	0.8	
	0.326	0.742	0.242	0.084		
	0.359	0.145	0.051	0.308		
	0.394	0.188	0.074	0.320	1.0	
	0.363	0.658	0.239	0.124		
	0.362	0.141	0.051	0.311		
	0.405	0.161	0.065	0.340	1.34	
	0.347	0.692	0.240	0.107		
	0.361	0.136	0.049	0.312		
	0.406	0.155	0.063	0.343	1.5	
	0.367	0.643	0.236	0.131		
	0.362	0.135	0.049	0.313		
	0.408	0.142	0.058	0.350	1.75	
	0.345	0.704	0.243	0.102		
	0.358	0.139	0.050	0.308		
	0.404	0.149	0.060	0.344	2.0	
	0.354	0.669	0.237	0.117		
	0.362	0.138	0.050	0.312		
2	0.375	0.128	0.048	0.327	all ε_{wf}	all ε_{ff}
	0.375	0.220	0.083	0.293	all ε_{wf}	all ε_{ff}
	0.391	0.220	0.086	0.305	all ε_{wf}	all ε_{ff}
3	0.375	0.075	0.028	0.346	all ε_{wf}	all ε_{ff}
	0.375	0.128	0.048	0.327	all ε_{wf}	all ε_{ff}
	0.391	0.220	0.086	0.305	all ε_{wf}	0
4	0.375	0.037	0.014	0.360	all ε_{wf}	all ε_{ff}
	0.375	0.128	0.048	0.327	all ε_{wf}	all ε_{ff}
	0.391	0.220	0.086	0.305	all ε_{wf}	0

The advantage of using DMD over traditional MD is that the particles do not need to be moved at short regularly spaced time steps as in traditional molecular dynamics. Instead, one only needs to calculate the time until the next collision for each particle, t_{ij}, and the particle's new postcollision velocity [32,33]. The collision time between particle i and all other particles $j \neq i$ is given by

$$t_{ij} = \frac{-|b_{ij}| \pm \sqrt{b_{ij}^2 - v_{ij}^2(r_{ij}^2 - \sigma^2)}}{v_{ij}^2}, \tag{3}$$

where $\boldsymbol{r}_{ij} \equiv \boldsymbol{r}_i$-$\boldsymbol{r}_j$ is their relative position, $\boldsymbol{v}_{ij} \equiv \boldsymbol{v}_i$-$\boldsymbol{v}_j$ is their relative velocity, and $\boldsymbol{b}_{ij} \equiv \boldsymbol{r}_{ij} \cdot \boldsymbol{v}_{ij}$ [31]. Next, the minimum collision time for the system, t_c, is chosen and all particles are moved according to

$$\mathbf{r}_i(t + t_c) = \mathbf{r}_i(t) + \mathbf{v}_i(t_c), \tag{4}$$

where $\boldsymbol{r}_i$ and $\boldsymbol{v}_i$ represent the i^{th} particle's position and velocity, respectively. At this point, exactly two particles collide while the remaining particles are separated from one another. New velocities for the colliding particles are calculated using conservation of momentum and of kinetic energy.

Our DMD simulations are carried out in a rectangular box ($L \times W \times H = 20 \times 10 \times 10\sigma_s$) with walls parallel to the yz plane and located at $x=-L/2$ and $x=L/2$. The box is periodic along the y and z axes. Since the diameter of species i is σ_i, only the width $(L-\sigma_i)$ is available to the particle centers. All the systems were equilibrated for 2 million collisions before the actual production run of 5 million collisions. Due to the large size of the files generated, the ensemble averages were calculated using trajectories of the particles that were recorded every 1,000 collisions. We calculated the density profiles by dividing the simulation box into a number of bins, in the direction perpendicular to the wall, and counting the number of small and big spheres in each bin.

In addition to the particle density profiles, we can extract various thermodynamic quantities from both the DMD simulations and the DFT calculations described below. In particular, we calculate the pressure, excess adsorption, and surface tension (surface excess free energy). In planar geometries, the pressure tensor contains two independent components only, the normal and transverse components. The former is determined by the condition for hydrostatic equilibrium [34],

$$p'_N(x) = -\rho(x)V'(x). \tag{5}$$

Integration of Eq. (5), from a specified point x_0 out into bulk fluid (e.g., $x=\infty$) where $V'(x)$ is zero and p_N is the bulk pressure p, yields

$$p = p_N(x_0) - \int_{x_0}^{\infty} dx \rho(x) V'(x). \tag{6}$$

Introduction of the external potential $V'(x)$ for each species into Eq. (6) results in the pressure sum rule. In our system, where the wall-small particle interaction is a square-well potential, we can calculate the bulk pressure from the contact peaks of the small and big sphere density profiles and from the second peak at $x=\lambda$ in the small particle density distribution [35]

$$\beta p = \rho_b(0) + \rho_s(0) - [\rho_s(x - \lambda^-) - \rho_s(x - \lambda^+)], \tag{7}$$

where $\beta = 1/kT$, k is Boltzmann's constant, and T is temperature. Here, $\rho_b(\sigma_b/2)$ and $\rho_s(\sigma_s/2)$ are the densities of big and small spheres at the wall, respectively, and λ^+ and λ^- correspond to the limits of approaching $x = \lambda$ from the right and left, respectively.

The excess adsorption of species i, $i = s$, b is defined as

$$\Gamma_i = \int_0^\infty dx[\rho_i(x) - \rho_{i,\ bulk}]. \tag{8}$$

Here we take the Gibbs dividing surface to be at $x = 0$ for all surface quantities, which is the natural choice for a mixture with different sphere sizes [10]. This definition is different than that used in some prior work in the literature for single component hard sphere fluids [34].

For a planar system the surface tension can be defined as the integral of the difference between the pressure tensor components [34],

$$\gamma = \int dx[p_N(x) - p_T(x)]. \tag{9}$$

It has been shown that the integral of $p_T(r)$ across a planar interface does not depend on the particular choice of pressure tensor [36] and, therefore, the surface tension γ is obtained directly from our simulations as [37]

$$\gamma = \frac{m}{2At} \sum \frac{(r_{ij}^2 - 3x_{ij}^2)}{2\sigma^2} B_{ij}, \tag{10}$$

where m is the mass of particle i, A is the surface area of the wall, r_{ij} is the distance between particles i and j, x_{ij} is the x component of the distance between particles i and j, and σ is the distance between the centers of particles. B_{ij} is evaluated at the collision between particles i and j as

$$B_{ij} = \begin{cases} b_{ij}; & \text{core} \\ \frac{1}{2}[(9\sigma^2\varepsilon/m + b_{ij}^2)^{1/2} + b_{ij}]; & \text{capture} \\ \frac{1}{2}[-(-9\sigma^2\varepsilon/m + b_{ij}^2)^{1/2} + b_{ij}]; & \text{dissociation} \\ b_{ij}; & \text{bounce,} \end{cases}$$

$$b_{ij} = r_{ij}(t)v_{ij}(t). \tag{11}$$

In the *capture* case, there is a soft-core collision between the particle and the wall and the particle is attracted toward the wall. In the *bounce* case, the cores collide and bounce off of each other. The factor of $\frac{1}{2}$ arises from the fact that there are two walls present in our systems; i.e., Eq. (10) is the surface tension of a single wall-fluid interface.

C. Classical density-functional theory

The generic methodology of classical DFT is built upon a mathematical theorem stating that in an open system specified by temperature T, total volume V, and chemical potentials of all constituent molecules μ_i, there is an invertible mapping between the external potential and the one-body density profiles [38–41]. In other words, there exists a density distribution $\rho_i(\boldsymbol{r})$ of the constituent species i that minimizes the functional $\Omega[\rho_i]$. This minimization is performed using a variational approach, while keeping chemical potential μ_i, volume V, and temperature T, constant, i.e., $(\delta\Omega[\rho_i]/\delta\rho_i)_{\mu,V,T} = 0$. This functional corresponds to the grand potential Ω of an open (μVT) ensemble. The grand potential for the binary fluid mixture is

$$\Omega[\rho_i(\mathbf{r})] = F_{id}[\rho_i(\mathbf{r})] + F_{hs}[\rho_i(\mathbf{r})] + F_{att}[\rho_{i=s}(\mathbf{r})] + \sum_{i=s,b} \int dr\rho_i(\mathbf{r})[V_i(\mathbf{r}) - \mu_i], \tag{12}$$

where the terms on the right hand side represent the intrinsic Helmholtz free energies for the ideal gas, hard spheres, and attractive interactions [42]. The final term is the Legendre transformation in which the μ_i are the species' chemical potentials and $V_i(\boldsymbol{r})$ is the external field due to the presence of surfaces in the system.

A precise expression of the intrinsic Helmholtz free energy as a functional of the molecular density profiles is generally unknown. Formulation of the Helmholtz energy functional is a task essentially equivalent to enumeration of the statistical partition function for the particular system under investigation. A viable approach is to divide the Helmholtz energy into an ideal part and an excess part. The ideal part represents the contribution of an ideal, noninteracting gas; the excess part accounts for interactions leading to the thermodynamic nonideality. The Helmholtz free energy for an ideal gas is given by

$$F_{id}[\rho_i(\mathbf{r})] = kT\sum_i \int d\mathbf{r}\rho_i(\mathbf{r})\{\ln[\Lambda_i^3\rho_i(\mathbf{r})] - 1\}, \tag{13}$$

where k is the Boltzmann constant, T is the temperature, and Λ_i is the thermal wavelength of the species i.

Here the hard sphere contribution to the free energy is computed using the fundamental measure theory (FMT) of Rosenfeld [16]. FMT DFTs are based on geometric interactions between the fluid components with a free-energy functional given by

$$F_{hs}[\rho_i(\mathbf{r})] = kT\int d\mathbf{r}\Phi[n_i(\mathbf{r})]. \tag{14}$$

The $n_i(\mathbf{r})$ are nonlocal weighted densities that are based on the deconvolution of the Mayer f function [43] for hard spheres into a sum of weighted functions based on the individual particle radii [16]. These are defined as

$$n_i(\mathbf{r}) = \sum_\alpha \int d\mathbf{r}'\rho_\alpha(\mathbf{r})\omega_\alpha^{(i)}(|\mathbf{r} - \mathbf{r}'|), \tag{15}$$

where the $\omega_\alpha^{(i)}$ are the weight functions:

$$w_3^i(\mathbf{r}) = \Theta(R_i - r),$$

$$w_2^i(\mathbf{r}) = \delta(R_i - r),$$

$$\vec{w}_2^i(\mathbf{r}) = \frac{\mathbf{r}}{r}\delta(R_i - r),$$

and $w_1^i(\mathbf{r})=w_2^i(\mathbf{r})/(4\pi R_i)$, $w_0^i(\mathbf{r})=w_2^i(\mathbf{r})/(4\pi R_i^2)$, and $\vec{w}_1^i(\mathbf{r})=\vec{w}_2^i(\mathbf{r})/(4\pi R_i)$. Here R_i is the radius of species i, $\Theta(r)$ is the Heaviside step function and $\delta(r)$ is the Dirac delta function. Several modifications to the original Rosenfeld FMT functional can be found in the literature [44,45]. The specific functional we used here, known as the "White-Bear" functional, was developed by Roth *et al.* [18]. It was designed to match the Mansoori-Carnahan-Starling-Leland (MCSL) equation of state [46] for multicomponent hard sphere fluids and is written as

$$\Phi = -n_0\ln(1-n_3) + \frac{n_1 n_2 - \vec{n}_1 \cdot \vec{n}_2}{1-n_3} + (n_2^3 - 3n_2\vec{n}_2 \cdot \vec{n}_2)\frac{n_3 + (1-n_3)^2\ln(1-n3)}{36\pi n_3^2(1-n_3)^2}. \quad (16)$$

For a more detailed derivation and discussion of FMT, we refer the reader to the recent review article by Roth [17].

Pairwise attractive interactions were implemented using a mean-field form for the Helmholtz free energy:

$$F_{att}[\rho(\mathbf{r})] = \frac{1}{2}\sum_i \sum_j \int d\mathbf{r}\int d\mathbf{r}'\rho_i(\mathbf{r})\rho_j(\mathbf{r})u_{ij}^{att}(|\mathbf{r}-\mathbf{r}'|), \quad (17)$$

where $u_{ij}^{att}(|\mathbf{r}-\mathbf{r}'|)$ is the attractive part of the pair potential in Eq. (2).

Minimization of the grand potential from Eq. (12) with respect to the density profiles of each fluid component produces a set of Euler-Lagrange equations which must be solved for all points in the computational volume. These are

$$\frac{\delta F[\rho_j]}{\delta \rho_i(\mathbf{r})} = \mu_i + V_i(\mathbf{r}), \quad (18)$$

where $F[\rho_i]=F_{id}[\rho_i]+F_{hs}[\rho_i]+F_{att}[\rho_i]$. The chemical potential of each species can be divided into its constituent parts, i.e., ideal, hard sphere, and attractions, and written as $\mu_i=\mu_i^{id}+\mu_i^{hs}+\mu_i^{att}$, where the superscripts indicate the contribution type.

Equation (18) is solved using the *Tramonto* [47] fluids-DFT code. The nonlinear integral equations are solved in real space on a Cartesian mesh using Newton's method as described previously [48–50]. The Jacobian matrix required in Newton's method is formed analytically, and we apply a segregated Schur complement technique to solve the linear matrix problem as detailed elsewhere [51]. In this paper, we are only concerned with fluids near a planar wall, and so the density profiles are only a function of the distance x from the surface. All of the DFT calculations presented here were therefore performed in a one-dimensional box of size $10\sigma_s$ for $\xi=2$ and $20\sigma_s$ for $\xi=3$ and 4, with a mesh size of $0.01\sigma_s$, and with a planar wall on one side of the computational domain. For convenience we used a reflective boundary on the other side of the domain; in all cases the density profiles reached their bulk values in the middle of the box.

The bulk pressure in the system was calculated from the density profiles using the pressure-sum rule given in Eq. (7). The numerical accuracy of the pressure calculations was confirmed (see the Appendix) by checking the values of the pressure obtained by Eq. (7) with the pressure calculated from the bulk equation of state in Tramonto. The excess adsorption was calculated from the density profiles obtained from DFT using Eq. (8). The excess surface free energy is defined as

$$\gamma = \frac{\Omega[\rho(x)]}{A} - \frac{\Omega_{bulk}}{A}, \quad (19)$$

where Ω is the grand free energy and Ω_{bulk} is the grand free energy of the bulk system at the same chemical potential as the inhomogeneous system.

III. RESULTS AND DISCUSSION

We present the results in two different sections. In the first section, we keep $\varepsilon_{ff}=0.0$ and study the effect of the wall-fluid attractions by increasing ε_{wf}. The DFT results for the $\xi=2$ case are compared with DMD simulations. In the second section, we add fluid-fluid attractions between the small spheres. In these results, all lengths are in units of σ_s and energies in units of kT.

A. Case 1: $\varepsilon_{ff}=0.0$

The number density profiles of both components of the binary mixture close to a planar wall were obtained from the DFT by a free minimization of the functional given in Eq. (12). For $\xi=2$ we also obtain density profiles from the DMD simulations. We calculated the densities of the small and big particles in the bulk region from the DMD simulations, and used those values in the DFT calculations in order to compare the two techniques. The relevant packing fractions are listed in Table I. Here, we present detailed results for the $\xi=2$ case only, as the results for $\xi=3$ and 4 are qualitatively similar.

We find excellent agreement between density functional theory and the simulations for the density profiles of both components for the $\xi=2$ system. In Fig. 2, we show the density profiles of the small and big spheres with two different wall-small particle attraction strengths, (a) $\varepsilon_{wf}=0.2$ and (b) $\varepsilon_{wf}=2.0$, to illustrate the agreement between the DFT and the DMD data. The high packing fraction of the system results in pronounced structure of the density profiles. For a weak wall-fluid attraction, the density of the big spheres near the wall is high, as seen by the tall peak in the density distribution, and is a result of the depletion effect caused by the size anisotropy. As ε_{wf} is increased, the peak corresponding to the density of the big spheres slowly diminishes, while a second peak in the density distribution of the small spheres begins to appear. The attraction between the wall and the small particles acts against the entropic force that arises due to the size anisotropy. This attraction pulls more small particles closer to the wall, dislodging the bigger particles. The location of the second peak in the density distribution of the

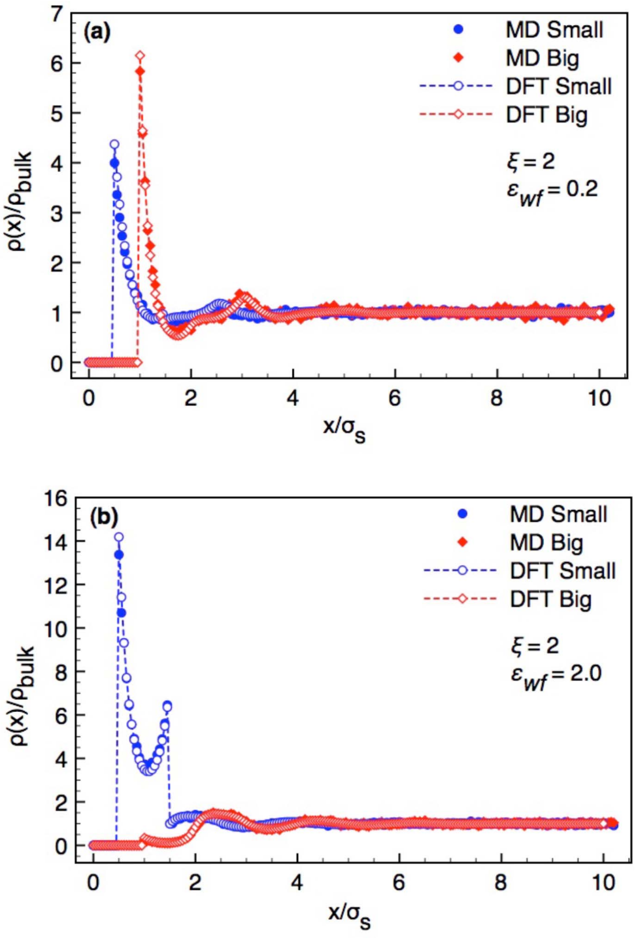

FIG. 2. (Color online) Density profiles for the small (blue circles) and large (red diamonds) particles with $\varepsilon_{ff}=0$ and $\xi=2$ for (a) $\varepsilon_{wf}=0.2$ and $\eta_s=0.084$ and (b) $\varepsilon_{wf}=2.0$ and $\eta_s=0.060$. Solid symbols are from DMD simulation and open symbols with dashed lines are from the DFT.

small particles corresponds to the range of the attractive wall potential.

A clearer way to see the effects of the wall-small particle attraction is to plot the local concentrations $C_s(x)$ and $C_b(x)$ of the small and large spheres, respectively, defined as

$$C_i(x) = \frac{\rho_i(x)}{\rho_s(x) + \rho_b(x)}, \quad i = s,b. \tag{20}$$

Figure 3 shows these concentration profiles for the same parameters as Fig. 2. These concentration profiles demonstrate that for the weak wall-small particle attraction, apart from the purely geometrical constraints, near the wall the big particles are enriched and the small particles are depleted. This result is similar to what is found for the purely hard sphere case where the gain in entropy of the small spheres induces an attractive depletion potential between the big spheres and the hard wall [10]. With a small value of ε_{wf}, the concentration of the big spheres near the wall is slightly lower than that of the hard-sphere case. For a stronger wall-small particle attraction, the enthalpic force due to the attraction between the small spheres and the wall dominates over the entropic force, resulting in the small spheres replacing the big spheres at the wall. This is clearly seen in Fig. 3(b), where the concentration of the small spheres is much higher than the concentration of the big spheres near the wall.

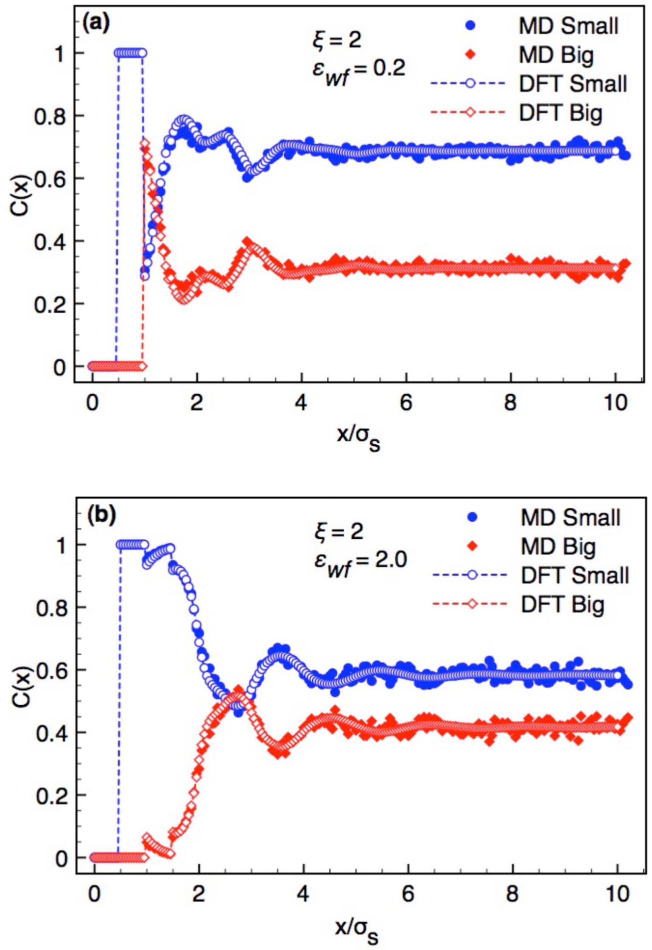

FIG. 3. (Color online) Concentration profiles for the small (blue circles) and large (red diamonds) particles with $\varepsilon_{ff}=0$ and $\xi=2$ for (a) $\varepsilon_{wf}=0.2$ and $\eta_s=0.084$ and (b) $\varepsilon_{wf}=2.0$ and $\eta_s=0.060$. Solid symbols are from DMD simulation and open symbols with dashed lines are from the DFT.

A similar result was observed recently by Zhou *et al.* [25], who investigated the effective interaction between a big hard sphere colloid, immersed in a sea of smaller hard particles, and a hard wall that has a different affinity to the small particles. They fixed the size ratio between the big and small colloids at $\xi=5$, and varied the interaction of the small particles with the wall from purely repulsive to attractive. When the wall is repulsive to the small particles, the effective large colloid-wall attractions are enhanced by depleted small particles near the wall. With an increase in the attractive strength between the wall and the small particles, a dense layer of small particles is formed near the wall, resulting in a high peak in the small particle density profile. Furthermore, this leads to an effective repulsion between the large particle and the wall, overcoming the depletion effect, analogous to the behavior we see in our system with a finite volume fraction of large spheres.

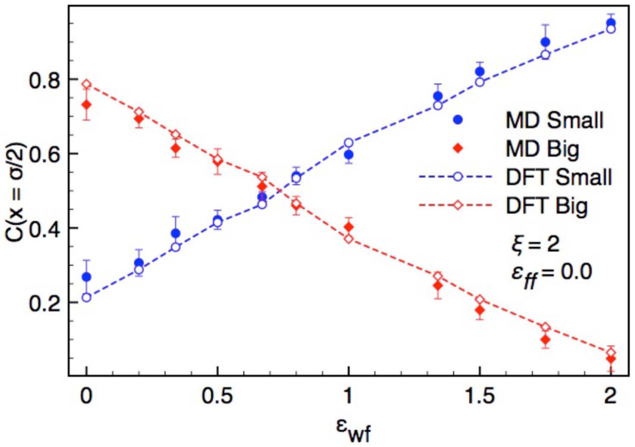

FIG. 4. (Color online) Concentrations of big (red diamonds) and small (blue circles) spheres near the wall, for $\varepsilon_{ff}=0$, $\xi=2$, and $\Phi_s \approx 0.22$. The increasing curve is for small spheres and the decreasing curve is for big spheres. The solid symbols are from MD simulations while open symbols with dashed curves are from DFT.

As ε_{wf} is increased in our system, there is a smooth transition in which the concentration of the big spheres at the wall falls while the concentration of the small spheres increases, as shown in Fig. 4. At $\varepsilon_{wf}^{*} \sim 0.7$, the concentrations of the small and big spheres near the wall are equal. Beyond this point, the attractive force existing between the small spheres and the wall dominates over the entropic force that is present due to the anisotropy in the sizes of the particles. We see good agreement between the simulations and the DFT results for the whole range of ε_{wf} values in Fig. 4.

Another way to quantify the numbers of particles near the wall is to calculate the excess adsorption. Figure 5 shows the excess adsorption of the small and big spheres, as calculated from Eq. (8), as a function of ε_{wf} for (a) different compositions for $\xi=2$, and (b) different size ratios at the same composition. For $\xi=2$ in Fig. 5(a), the bulk densities used in the DFT calculation for each ε_{wf} were taken from the MD results. All of the calculations for $\xi=2$, 3, and 4 in Fig. 5(b) were carried out at the same total packing fraction of 0.391, with $\phi_s=0.22$ (see Table I), using only the DFT. Because the excess adsorptions follow from integrating over oscillatory functions, they depend very sensitively on the precise structure of the density profiles and this makes them a very good measure for comparison between the simulations and the DFT calculations. Figure 5(a) shows good agreement between DFT and DMD for all three compositions. For all the systems studied here, the adsorption of small spheres increases and the adsorption of big spheres decreases as we increase ε_{wf}. In Fig. 5(b), we note that for increasing size ratios, the change in the excess adsorption of the big spheres with increasing ε_{wf} is less. This is because the depletion effect is stronger for larger size ratios, and so applying the wall-fluid attraction has less of an effect.

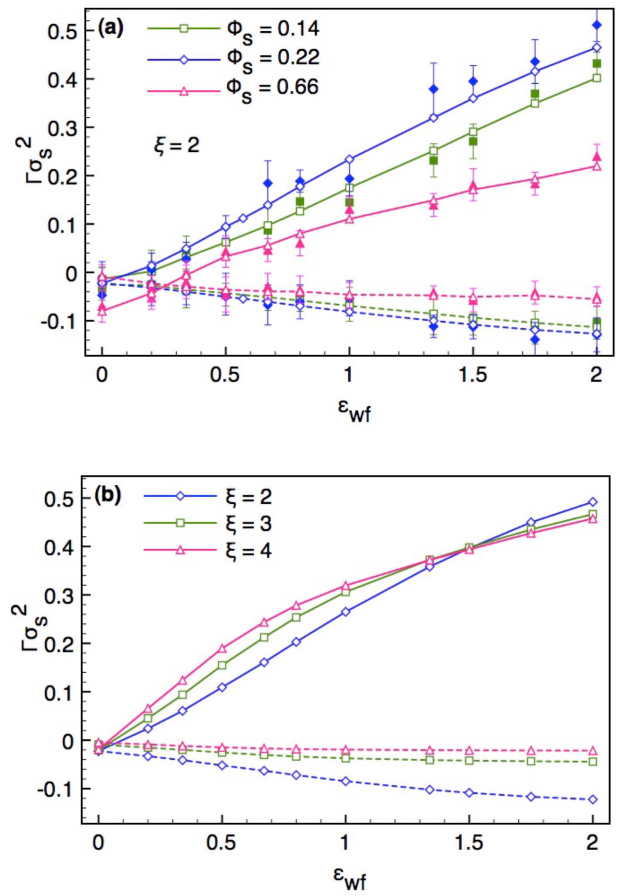

FIG. 5. (Color online) Excess adsorption at $\varepsilon_{ff}=0$ as a function of ε_{wf} for (a) $\xi=2$ at different compositions, and (b) different size ratios at the same composition with $\Phi_s=0.22$ (total packing fraction $\eta=0.391$). Increasing (solid) curves are for the small spheres, while decreasing (dashed) curves are for the large spheres. Solid symbols are from MD simulations; curves with open symbols are DFT calculations.

Surface tensions are not often reported in the literature, but are also a sensitive test of the agreement between DFT and simulation. Hence we calculated the surface tension for systems with $\varepsilon_{ff}=0.0$ using both methods, as shown in Fig. 6 for the same parameters as in Fig. 5. The surface tension decreases as the wall-fluid attraction is increased, since the wall-fluid attraction makes it more favorable to have the wall present in the system. For the systems with $\phi_s \approx 0.14$ and $\phi_s \approx 0.22$ shown in Fig. 6(a), the packing fraction and hence the number of the large spheres is approximately the same. The slopes of the surface tension and adsorption curves are roughly the same in these two cases, whereas for the third composition where the packing fraction of large spheres is different, the slope is quite different. Once again we obtain excellent agreement between DFT and DMD. For different size ratios at a constant small sphere volume fraction of $\phi_s \approx 0.22$ as in Fig. 6(b), we find that the slopes of all three curves are again roughly similar, with the curves just shifted along the vertical axis.

The qualitative behavior of the system is the same if the range of the wall-fluid interactions is increased to $\lambda=2.5$. This is demonstrated in Fig. 7 which shows the concentration of the small and big spheres near the wall for various wall-fluid attractions with both $\lambda=1.5$ (with $\phi_s \approx 0.22$) and $\lambda=2.5$ (with $\eta=0.388$ and $\phi_s=0.214$). The value of ε_{wf}^{*} is lower in the case of $\lambda=2.5$ since it is easier to pull more

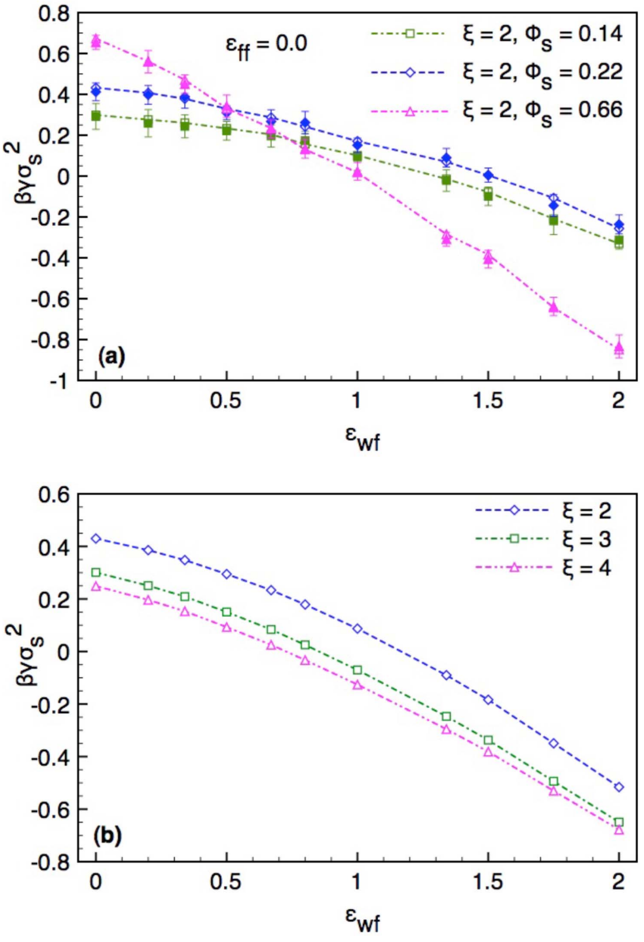

FIG. 6. (Color online) Surface tension at $\varepsilon_{ff}=0$ as a function of ε_{wf} for (a) $\xi=2$ at different compositions, and (b) different size ratios at the same composition $\Phi_s=0.22$ (total packing fraction $\eta=0.391$). Solid symbols in (a) are from MD simulations.

small particles close to the wall with a larger range of attraction.

B. Case 2: nonzero ε_{ff}

In this section we consider the effects of adding fluid-fluid attractions between the small spheres, using the square-well fluid-fluid attraction as given in Eq. (2). Here we are only interested in miscible systems that are far from any phase boundaries, so we calculated liquid-vapor phase diagrams from our DFT [52]. First we calculated the phase diagram for a pure (single component) square-well fluid and compared it to simulation results from the literature [53,54]. As previously observed by Gloor *et al.* [54] for the same equation of state applied to the same square-well fluid, the theory underestimates the location of the vapor-liquid critical point and the width of the coexistence curve (see Fig. 1 in [54] for a comparison of the mean-field DFT coexistence curve and simulation results). This is because the mean-field treatment of the attractions cannot accurately describe the coexistence curve. For our binary mixture of hard spheres and a square-well fluid, we can compare to Gibbs ensemble Monte Carlo simulations of Green *et al.* [55], for the case of equal sized spheres, $\xi=1$. Once again, our equation of state leads to an underprediction of the critical point (we obtain a critical point near $\varepsilon_{ff}=1.33$ compared to the simulation result of $\varepsilon_{ff}=1.5$) and a downward (in ε_{ff}) shift of the whole phase envelope, due to the inaccuracy of the mean-field attractions in predicting the vapor-liquid phase behavior. We therefore cannot expect good agreement between DFT and DMD simulations anywhere near the coexistence curves in our systems.

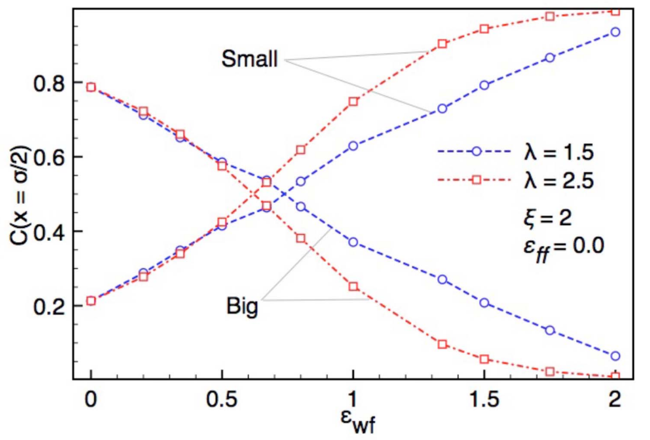

FIG. 7. (Color online) Concentration near the wall for $\lambda=1.5$ (blue circles) and $\lambda=2.5$ (red squares) as a function of ε_{wf}, with $\xi=2$ and $\varepsilon_{ff}=0$.

In this section, the values for ε_{ff} have been chosen such that the two components are completely miscible in all proportions; we keep $\varepsilon_{ff} \leq 0.4$ in all calculations. We note that the coexistence curve is typically calculated in ε_{ff}-composition space at constant pressure, whereas in our DFT calculations for the mixture near a wall, we keep the composition fixed and vary ε_{ff}, which also leads to variation in the pressure. For all our systems, the two-phase region is larger and the critical point lower in ε_{ff} as the pressure increases. Therefore, we calculated phase diagrams at the highest possible pressure for a given composition of interest, which is the pressure when $\varepsilon_{ff}=0$ at that particular compo-

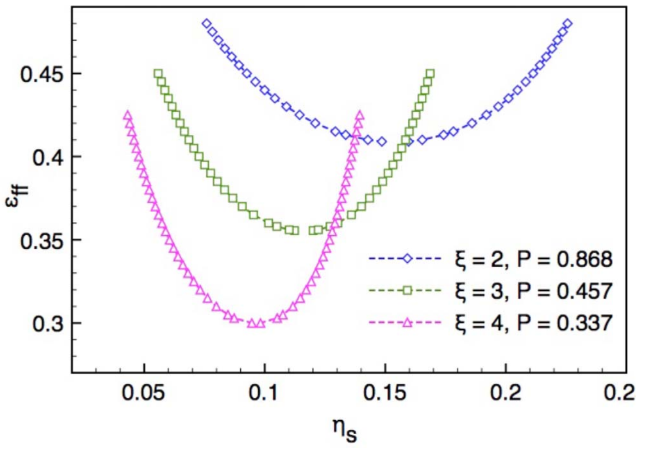

FIG. 8. (Color online) Coexistence curves for $\xi=2$, 3, and 4 at pressures of $p=0.868$, 0.457, and 0.337, respectively (pressure in units of kT/σ_s^3).

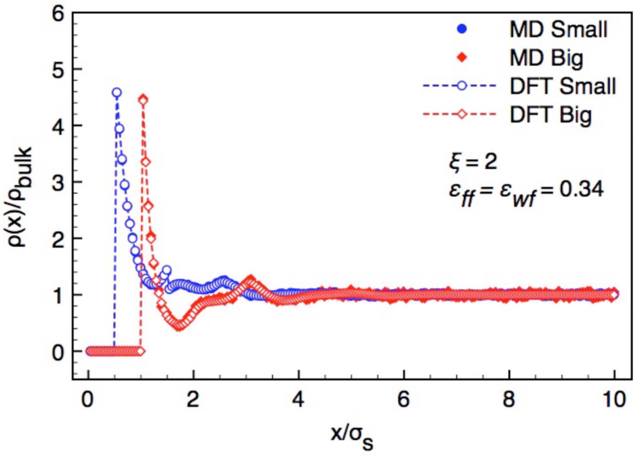

FIG. 9. (Color online) Density profiles for the small (blue circles) and large (red diamonds) spheres with ξ=2 and $\sigma_s \approx 0.22$, for $\varepsilon_{ff}=\varepsilon_{wf}=0.34$. Solid symbols are from DMD simulation and open symbols with dashed lines are from the DFT.

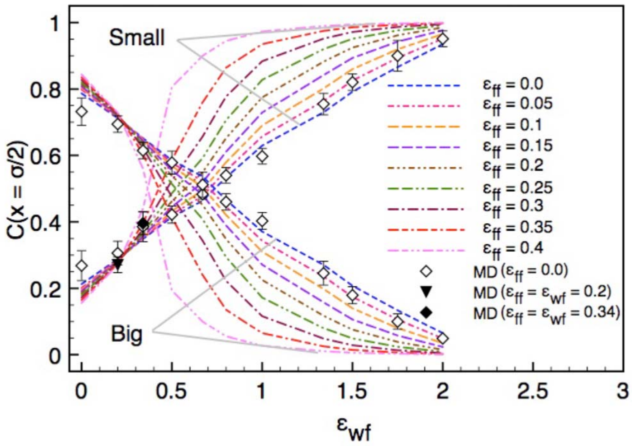

FIG. 10. (Color online) Concentration near the wall as a function of ε_{wf}, for different fluid-fluid attraction strengths for ξ=2 and $\sigma_s \approx 0.22$. The symbols are from MD simulations. Open symbols are for ε_{ff}=0.0 and solid symbols are for $\varepsilon_{ff}=\varepsilon_{wf}$.

sition. We then verified that each composition we used was well outside the two-phase boundary at that pressure. Figure 8 shows some representative vapor-liquid coexistence curves for ξ=2, 3, and 4. For these curves the pressure was chosen based on the mixtures with total packing fractions of η =0.375 and $\phi_s \approx 0.128$. Clearly for ξ=2, the mixture is miscible for all compositions when $\varepsilon_{ff} \leq 0.4$. For the larger size ratios, we only consider compositions that are outside the two-phase region, with $\eta_s < 0.05$ for ξ=3 and 4 at η =0.375 (see compositions in Table I).

We simulated two systems with both wall-fluid and fluid-fluid attractions at ξ=2 and $\phi_s \approx 0.22$, setting $\varepsilon_{wf}=\varepsilon_{ff}=0.34$ and $\varepsilon_{wf}=\varepsilon_{ff}=0.2$ (and also verified that these mixtures are well outside the two-phase region). We find excellent agreement between DFT and DMD for the density profiles for both these cases, as illustrated in Fig. 9 for the $\varepsilon_{wf}=\varepsilon_{ff}$ =0.34 case. This excellent agreement between theory and simulation is due to several reasons. First, we matched the bulk densities away from the wall in both calculations. Second, since the strength of attraction in these systems is fairly low, the inaccuracy that results from the mean-field term is also minimal. At these compositions, we are far away from the coexistence region and the packing effects dominate over the attractive fluid-fluid interactions. Finally, we also have an attractive wall-fluid interaction, which additionally improves agreement between DFT and simulation as seen in previous work [19–21]. It therefore appears that in these circumstances, the mean-field approach is sufficient. Table II shows the comparison between the theory and simulations for the surface tension and excess adsorptions for these systems.

Figure 10 shows the concentrations of the small and big spheres at the wall as a function of ε_{wf} for various values of ε_{ff} for ξ=2 and Φ_s=0.22. The transitional value ε^*_{wf} drops to lower values as the fluid-fluid attractions get stronger, meaning that a weaker wall-small particle attraction is required to push the large particles off the wall when there are also attractions between the small particles. This counterintuitive effect can be understood by the fact that the wall-fluid attraction leads to an enhancement of the particles near the wall, and an additional fluid-fluid attraction then pulls even more of them into those peaks since the small particles want to be near each other at nonzero ε_{ff}. This effect was also seen by Karanikas *et al.* [21], who observed a nonlinear enhancement of particle densities near the wall (compared to the case of hard spheres near a hard wall) for a fluid with both fluid-fluid and wall-fluid attractive interactions. This phenomenon leads to a decrease in the wall-fluid attraction required to obtain a 50–50 concentration of the particles near the wall as ε_{ff} is increased.

Finally, Fig. 11 shows the transitional wall-fluid attraction strength ε^*_{wf} as a function of fluid-fluid attraction strength ε_{ff} for the three different size ratios, at a fixed total packing fraction of η=0.375. Figure 11(a) shows ε^*_{wf} as a function of

TABLE II. Comparison of excess adsorption and surface tension between DFT and DMD.

		DFT		MD	
	$\varepsilon_{wf}=\varepsilon_{ff}$	Small	Big	Small	Big
Excess adsorption	0.20	0.02252	−0.03299	0.02113	−0.03424
	0.34	0.12337	−0.05597	0.11935	−0.05734
Surface tension	0.20	0.39033		0.38412	
	0.34	0.35838		0.34141	

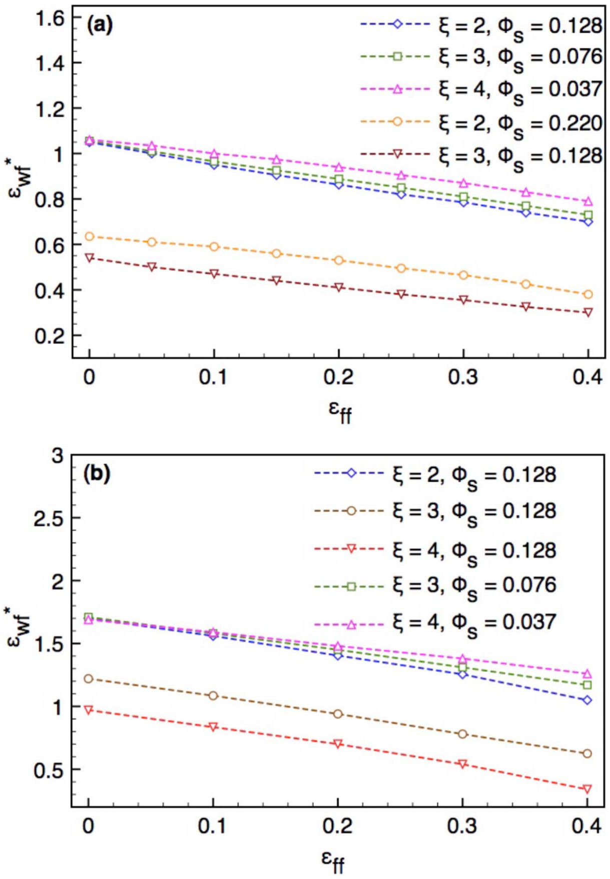

FIG. 11. (Color online) ε_{wf}^* as a function of ε_{ff} at a constant total packing fraction of η=0.375 for different size ratios and compositions with (a) the concentration criterion and (b) the density criterion for ε_{wf}^* as described in the text.

ε_{ff}, calculated as before from the value of ε_{wf} when the concentrations of big and small spheres at the wall are equal. In the top set of curves, the compositions for ξ=3 and 4 have been adjusted such that the value of ε_{wf}^* coincides with the value of ε_{wf}^* for ξ=2 (at Φ_s=0.128) when ε_{ff}=0.0. We note that the slope of the ε_{wf}^* *vs.* ε_{ff} curve is smaller for larger size asymmetries. The nonlinear enhancement effect discussed above, which lowers ε_{wf}^* with increasing fluid-fluid attraction strength ε_{ff}, appears to be less effective as the size asymmetry increases. This could be because the depletion attraction between the large sphere and the wall is stronger for stronger size asymmetries. It may also be because the small sphere number density decreases for these three cases, from $\rho_s\sigma_s^3$ =0.092 for ξ=2, to $\rho_s\sigma_s^3$=0.054 for ξ=3 and $\rho_s\sigma_s^3$=0.026 for ξ=4, so the total effect of the fluid-fluid attractions is less. At the same fixed composition of Φ_s=0.128 with the same number of small particles, the curve for ξ=3 is well below that of ξ=2; because of the larger size asymmetry, here there are fewer large particles in the ξ=3 case, and it apparently requires less wall-fluid attraction to displace them from the wall even though one would expect the depletion attraction to be stronger. Figure 11(a) also shows for both ξ=2 and ξ =3 that the values of ε_{wf}^* are lower for a larger volume fraction of small spheres, but the dependence on ε_{ff} is similar.

Finally, we investigated using a different criterion for defining the transitional wall-fluid attraction strength. Using our original concentration-based criterion for ε_{wf}^*, when the number density of the big spheres is too low, the concentration of the small spheres next to the wall is larger than that of the big spheres even for very small ε_{wf}. As a result, it is impossible to identify ε_{wf}^* in these cases from the concentrations at the wall. Nevertheless, in these systems the big spheres still experience a depletion potential and get pushed preferentially toward the wall. An alternative criterion is to determine the value of ε_{wf} when the density of the large spheres at the wall is equal to their density in the bulk, $\rho_b^{wall}/\rho_b^{bulk}$=1. For weak ε_{wf} we expect $\rho_b^{wall}>\rho_b^{bulk}$, reflecting the enhancement of the large spheres at the wall; as they are displaced by the small spheres, we should eventually find $\rho_b^{wall}<\rho_b^{bulk}$. The results of using this new criterion are shown in Fig. 11(b). The new criterion allows us to identify ε_{wf}^* for

TABLE III. Pressure obtained from DMD, from DFT using the bulk equation of state (EOS), and from DFT using the sum rule in Eq. (7), for small particle volume fractions Φ_s=0.14, 0.22, and 0.66, at various values of the small particle-wall attraction strength ε_{wf}.

	βp								
	Φ_s=0.14			Φ_s=0.22			Φ_s=0.66		
ε_{wf}	DMD	DFT (bulk EOS)	DFT (sum rule)	DMD	DFT (bulk EOS)	DFT (sum rule)	DMD	DFT (bulk EOS)	DFT (sum rule)
0.0	0.8132	0.7419	0.7408	1.2512	1.2534	1.2526	2.2453	2.4214	2.4050
0.2	0.8468	0.7792	0.7784	1.2381	1.2443	1.2249	2.2723	2.2887	2.2844
0.34	0.8132	0.7806	0.7919	1.2364	1.2547	1.2389	2.3123	2.3566	2.3278
0.5	0.7704	0.8179	0.7963	1.2516	1.2323	1.2405	2.1023	2.1009	2.1053
0.67	0.8912	0.8356	0.8403	1.2113	1.2363	1.2214	2.3644	2.2373	2.2919
0.8	0.8418	0.7985	0.7840	1.2426	1.2266	1.2255	2.3584	2.0341	2.1027
1.0	0.8154	0.8153	0.8152	1.2193	1.2034	1.2064	2.3134	2.2668	2.3059
1.34	0.8129	0.7939	0.7971	1.2124	1.2173	1.2147	2.2934	2.1833	2.1857
1.5	0.8348	0.7998	0.7973	1.2347	1.2136	1.2363	2.2725	2.2586	2.2636
1.75	0.8419	0.7818	0.7932	1.2114	1.1862	1.2135	2.3265	2.2445	2.2434
2.0	0.8671	0.8017	0.8132	1.2137	1.1698	1.2121	2.3554	2.3087	2.3086

mixtures with $\xi=4$ and $\Phi_s=0.128$, which was not possible with the concentration-based criterion. With this density-based criterion, the values of ε_{wf}^* are higher than they are for the concentration criterion used in Fig. 11(a). The trends remain the same; in particular, at fixed composition the values of ε_{wf}^* decrease with increasing size asymmetry, again apparently because the number of large spheres decreases and they are easier to displace from the wall.

IV. SUMMARY AND CONCLUSIONS

We have analyzed the structural and thermodynamic properties of a binary fluid mixture near a planar wall with wall-small particle and small particle fluid-fluid attractions, using both DFT and DMD simulations. For hard sphere mixtures with small particle-wall attractions, we find excellent agreement between the DFT and DMD results for density profiles, excess adsorption, and surface tension. Adding fluid-fluid attractions between the small spheres by including a mean-field attraction in the DFT, we also find good agreement with DMD for state points that are far from any phase coexistence boundaries. The good agreement in this case, despite the shortcomings of the mean-field approximation in the DFT, is due to the fact that the bulk densities of both components away from the wall were matched and at these compositions, packing effects dominate over the attractions.

We showed, for purely hard sphere mixtures, that adding an attractive interaction between the small particles and the wall overcomes the entropic depletion force that causes enhancement of the big spheres at the wall for small values of ε_{wf}; for larger values of ε_{wf}, the small particles displace the large particles from the wall. Defining the transition value of ε_{wf}^* as that value of ε_{wf} where the concentrations of big and small spheres at the wall are equal, we find that ε_{wf}^* is on the order of the thermal energy kT for the range of systems studied here.

When there are also attractions between the small spheres, there is a decrease in ε_{wf}^*. This is due to a nonlinear enhancement of the adsorption of the small spheres [21]: the attractive interaction with the wall causes an increase in the number of small particles near the wall, which is then further increased due to the fluid-fluid interaction attracting even more small particles into the near-wall density peaks. Not surprisingly for a quantity that depends on the interplay between entropic and enthalpic effects, the behavior of the transition value ε_{wf}^* also depends on the size ratio ξ and the absolute number densities of large and small particles.

ACKNOWLEDGMENTS

The authors would like to thank the U.S. Department of Energy for funding this research. This work was performed, in part, at the Center for Integrated Nanotechnologies, a U.S. Department of Energy, Office of Basic Energy Sciences user facility at Los Alamos National Laboratory (Contract No. DE-AC52-06NA25396) and Sandia National Laboratories (Contract No. DE-AC04-94AL85000).

APPENDIX

As an additional comparison between the DFT and DMD simulations, in Table III we show the bulk pressure for different ε_{wf} and the three different compositions studied, for the $\xi=2$ case. For the DFT results we calculated the pressure both from the sum rule of Eq. (7) and from the bulk equation of state in the DFT. The pressures as obtained from DFT and DMD are in good agreement with each other. Additionally, the agreement in the two different calculations of the pressure from the DFT is reasonable, indicating that our numerical methods are sound. We note that decreasing the mesh size further improves the consistency between these two pressure calculations.

---

[1] A. Lajovic, M. Tomsic, and A. Jamnik, Acta Chim. Slov. **56**, 145 (2009).

[2] R. S. Krishnan *et al.*, Nano Lett. **7**, 484 (2007).

[3] P. D. Kaplan, J. L. Rouke, A. G. Yodh, and D. J. Pine, Phys. Rev. Lett. **72**, 582 (1994).

[4] Z. Tan, U. M. B. Marconi, F. van Swol, and K. E. Gubbins, J. Chem. Phys. **90**, 3704 (1989).

[5] S. Sokolowski and J. Fischer, Mol. Phys. **70**, 1097 (1990).

[6] A. R. Denton and N. W. Ashcroft, Phys. Rev. A **44**, 8242 (1991).

[7] W. C. K. Poon and P. B. Warren, EPL **28**, 513 (1994).

[8] A. D. Dinsmore, A. G. Yodh, and D. J. Pine, Phys. Rev. E **52**, 4045 (1995).

[9] J. P. Noworyta, D. Henderson, S. Sokolowski, and K.-Y. Chan, Mol. Phys. **95**, 415 (1998).

[10] R. Roth and S. Dietrich, Phys. Rev. E **62**, 6926 (2000).

[11] A. D. Dinsmore, P. B. Warren, W. C. K. Poon, and A. G. Yodh, EPL **40**, 337 (1997).

[12] H. N. W. Lekkerkerker and A. Stroobants, Physica A **195**, 387 (1993).

[13] A. Ayadim and S. Amokrane, Phys. Rev. E **74**, 021106 (2006).

[14] P. D. Kaplan, L. P. Faucheux, and A. J. Libchaber, Phys. Rev. Lett. **73**, 2793 (1994).

[15] A. D. Dinsmore, A. G. Yodh, and D. J. Pine, Nature (London) **383**, 239 (1996).

[16] Y. Rosenfeld, Phys. Rev. Lett. **63**, 980 (1989).

[17] R. Roth, J. Phys.: Condens. Matter **22**, 063102 (2010).

[18] R. Roth, R. Evans, A. Lang, and G. Kahl, J. Phys.: Condens. Matter **14**, 12063 (2002).

[19] A. L. Frischknecht and J. G. Curro, J. Chem. Phys. **121**, 2788 (2004).

[20] A. A. Louis, E. Allahyarov, H. Löwen, and R. Roth, Phys. Rev. E **65**, 061407 (2002).

[21] S. Karanikas, J. Dzubiella, A. Moncho-Jordá, and A. A. Louis, J. Chem. Phys. **128**, 204704 (2008).

[22] P. I. Ravikovitch, A. Vishnyakov, and A. V. Neimark, Phys. Rev. E **64**, 011602 (2001).

[23] Y. X. Yu, F. Q. You, Y. Tang, G. H. Gao, and Y. G. Li, J. Phys. Chem. B **110**, 334 (2006).

[24] F. Q. You, Y. X. Yu, and G. H. Gao, J. Phys. Chem. B **109**,

3512 (2005).

[25] L. Zhou, Y. Jiang, Y. Wang, and Y. Ma, Physica A **388**, 1359 (2009).

[26] R. L. C. Vink, K. Binder, and H. Lowen, J. Phys.: Condens. Matter **20**, 404222 (2008).

[27] P. Germain and S. Amokrane, Phys. Rev. E **76**, 031401 (2007).

[28] R. L. C. Vink, A. De Virgiliis, J. Horbach, and K. Binder, Phys. Rev. E **74**, 031601 (2006).

[29] D. C. Rapaport, J. Phys. A **11**, L213 (1978).

[30] D. C. Rapaport, J. Chem. Phys. **71**, 3299 (1979).

[31] S. W. Smith, C. K. Hall, and B. D. Freeman, J. Comput. Phys. **134**, 16 (1997).

[32] M. P. Allen and D. J. Tildesley, *Computer Simulation of Liquids* (Clarendon, Oxford, 1987).

[33] J. M. Haile, *Molecular Dynamics Simulation* (Wiley, New York, 1992).

[34] J. R. Henderson and F. van Swol, Mol. Phys. **51**, 991 (1984).

[35] F. van Swol and J. R. Henderson, J. Chem. Soc., Faraday Trans. 2 **82**, 1685 (1986).

[36] P. Schofield and J. R. Henderson, Proc. R. Soc. London, Ser. A **379**, 231 (1982).

[37] J. R. Henderson and F. van Swol, Mol. Phys. **56**, 1313 (1985).

[38] P. Hohenberg and W. Kohn, Phys. Rev. **136**, B864 (1964).

[39] R. Evans, Adv. Phys. **28**, 143 (1979).

[40] N. D. Mermin, Phys. Rev. **137**, A1441 (1965).

[41] J. Wu and Z. Li, Annu. Rev. Phys. Chem. **58**, 85 (2007).

[42] G. J. Gloor, F. J. Blas, E. M. del Rio, E. de Miguel, and G. Jackson, Fluid Phase Equilib. **194-197**, 521 (2002).

[43] H. T. Davis, *Statistical Mechanics of Phases, Interfaces, and Thin Films* (VCH, New York, 1996).

[44] Y. Rosenfeld, M. Schmidt, H. Löwen, and P. Tarazona, Phys. Rev. E **55**, 4245 (1997).

[45] H. Hansen-Goos and R. Roth, J. Phys.: Condens. Matter **18**, 8413 (2006).

[46] G. A. Mansoori, N. F. Carnahan, K. E. Starling, and J. T. W. Leland, J. Chem. Phys. **54**, 1523 (1971).

[47] See http://software.sandia.gov/tramonto.

[48] L. J. D. Frink and A. G. Salinger, J. Comput. Phys. **159**, 407 (2000).

[49] L. J. D. Frink and A. G. Salinger, J. Comput. Phys. **159**, 425 (2000).

[50] L. J. D. Frink, A. G. Salinger, M. P. Sears, J. D. Weinhold, and A. L. Frischknecht, J. Phys.: Condens. Matter **14**, 12167 (2002).

[51] M. Heroux, A. G. Salinger, and L. J. D. Frink, SIAM J. Sci. Comput. (USA) **29**, 2059 (2007).

[52] Setting the densities $\rho_i(x)=\rho_{ib}$, their constant bulk value, in the free energy of Eq. (12) allows us to calculate the bulk pressure p from $-pV=\Omega$ and the chemical potentials from Eq. (18). The equation of state is simply the MCSL mixture equation of state [46] plus the mean-field attractive contribution. The phase diagram is determined by requiring the pressure and the two species' chemical potentials to be equal in both phases.

[53] L. Vega, E. de Miguel, L. F. Rull, G. Jackson, and I. A. McLure, J. Chem. Phys. **96**, 2296 (1992).

[54] G. J. Gloor, G. Jackson, F. J. Blas, E. M. del Rio, and E. de Miguel, J. Chem. Phys. **121**, 12740 (2004).

[55] D. G. Green, G. Jackson, E. de Miguel, and L. F. Rull, J. Chem. Phys. **101**, 3190 (1994).